



UNIVERSITY OF TRENTO  
DEPARTMENT OF PHYSICS  
BACHELOR'S DEGREE IN PHYSICS

~ . ~

ACADEMIC YEAR 2023–2024

# BUBBLES IN A FERROMAGNETIC SUPERFLUID

**Supervisor**  
Dr. Alessandro ZENESINI

**Graduate Student**  
Giorgio MICAGLIO  
227051

FINAL EXAMINATION DATE: March 10, 2025

---



---

*A mamma e papà*



# Acknowledgments

I would first like to thank my parents, that encouraged me to pursue my study path and supported me throughout its entirety.

Then, a much needed thanks goes to all of my friends I met here in Trento: the *AISF local committee* members, *Gli scalatori di Povo*, the *Lunedì* roommates.

A special thanks is for my dear friends of *Stasssse* Anna, Caterina, Federico, Gabriele, Giacomo, Giulia, Matteo and Roberto, with whom I shared the most unforgettable moments of my Bachelor years, for which I will always be grateful.

I would also like to thank my supervisor, dr. Alessandro Zenesini, who provided me with the idea and the data for this thesis, along with all the great support in developing the methods used for the analysis.



## **Abstract**

This thesis investigates the characteristic features of bubbles in a ferromagnetic superfluid, which form by false vacuum decay. The primary objective is to analyze the experimental data to identify and quantify the key properties of these bubbles. By examining the relationship between the experimental parameters and the observed bubble characteristics, this work aims to provide a deeper understanding of the underlying physical phenomena and contribute to the broader fields of ferromagnetism and superfluidity.



# Contents

<b>Introduction</b>	<b>1</b>
<b>1 Theoretical background</b>	<b>3</b>
1.1 Ideal Bose gas . . . . .	3
1.2 Gross-Pitaevskii equation . . . . .	5
1.3 Two-component mixture . . . . .	5
1.4 Coherently coupled mixture . . . . .	7
1.4.1 Ferromagnetism . . . . .	7
1.5 False vacuum decay and bubble formation . . . . .	8
<b>2 Data analysis</b>	<b>11</b>
2.1 Experimental platform . . . . .	11
2.2 Raw data . . . . .	12
2.2.1 Bubble fit parameters . . . . .	12
2.2.2 Shot sorting . . . . .	14
2.3 Parameters analysis . . . . .	14
2.4 Spectral analysis . . . . .	15
2.4.1 FFT and ACF definition . . . . .	16
2.4.2 FFT and ACF analysis on sequences . . . . .	18
2.4.3 ACF analysis on all shots . . . . .	19
<b>Conclusions</b>	<b>25</b>
<b>A ACF model</b>	<b>27</b>
<b>Bibliography</b>	<b>29</b>
<b>List of Figures</b>	<b>32</b>

## CONTENTS

---

# Introduction

This thesis originates from the first experimental observation of the false vacuum decay (FVD) via bubble formation phenomenon, made in the Pitaevskii BEC Center laboratories of the University of Trento and presented in Ref. [7]. This process is a direct consequence of metastability, namely the finite lifetime of a state when a lower-energy configuration exists but can be reached only through the tunnelling of an energy barrier. FVD is a widely studied phenomenon, explored from a theoretical standpoint in a variety of energy and length scales: from quantum many-body systems to protein-folding and cosmology. However, since in the cosmological case the energy scales are experimentally unavailable, dealing with smaller scales may be the right path to observe and characterize the process.

The framework of the experiment in Trento is of quantum nature and relies on a ferromagnetic superfluid mixture of Bose-Einstein condensates, specifically a system of Sodium atoms optically trapped and cooled below the condensation temperature, forming a two-component spin mixture. The superfluidity of the system guarantees its spatial coherence and thus that it behaves as a single quantum field. The ferromagnetism is a consequence of the double-well energy landscape.

The purpose of this work is to characterize the bubbles formed during the decay process by analyzing the magnetization of the system. The goal is to study the bubble properties such as its location and spatial extension in the condensate in relation to the experimental parameters, controlled and tuned in the laboratory apparatus, but also to the evolution of the system.

In the first chapter, a quick theoretical background on the quantum properties of our system will be provided, where we will introduce the condensation phenomenon through the simple case of the ideal Bose gas and then add the interaction component with the Gross-Pitaevskii equation. We will then describe the properties of a two-component mixture alone and in the presence of a coherent coupling between the species, that enables ferromagnetism. We will conclude with a brief explanation of how bubbles form and evolve in FVD, along with some experimental remarks.

In the second chapter we will focus instead on the main work of this thesis: the analysis of the experimental data. We will begin by extracting the visible bubble parameters from the images of the system and then proceed with their analysis. Successively, a spectral analysis will be performed on the bubbles for a further exploration of their properties.

Eventually, we will draw conclusions on our work and evaluate if the adopted procedures produced physically reasonable results and contributed to the experimental study of the phenomenon.

## INTRODUCTION

---

# Chapter 1

## Theoretical background

In this chapter we will briefly discuss the theoretical background used when dealing with two-component coherently coupled spin mixtures of BECs. Since we are dealing with a many-body quantum problem, the standard approach is to use a quantum field to describe the state of the condensate. This leads directly to the Gross-Pitaevskii equation, which will be the starting point of this discussion, after a quick review of the ideal Bose gas. The following content is mostly based on Refs. [6] and [5].

### 1.1 Ideal Bose gas

The simplest way to treat the ideal Bose gas (a quantum system of non-interacting bosons) is by relying on the grand-canonical ensemble.

Let us then recall the probability of the system having a number of particles  $N'$  and energy  $E_k$  when in contact with a reservoir of temperature  $T$  and chemical potential  $\mu$ :

$$P_{N'}(E_k) = e^{\beta(\mu N' - E_k)},$$

with  $\beta = 1/(k_B T)$ , from which one can build the *grand-canonical partition function*

$$\mathcal{Z}(\beta, \mu) = \sum_{N'=0}^{\infty} \sum_k P_{N'}(E_k) = \sum_{N'=0}^{\infty} e^{\beta\mu N'} Q_{N'}(\beta), \quad (1.1)$$

where  $Q_{N'}$  is the canonical partition function associated to a system of  $N'$  (fixed) particles. From the partition function, the physical properties of the system are derived through the calculation of the grand-canonical potential

$$\Omega = E - TS - \mu N = -k_B T \log \mathcal{Z}. \quad (1.2)$$

In the case of a non-interacting system, the total Hamiltonian is  $H = \sum_i H_i$ , where the single-particle Hamiltonian solves the eigenvalue problem  $H_i \phi_i(\mathbf{r}) = \epsilon_i \phi_i(\mathbf{r})$ . In this setting, each energy level  $\epsilon_i$  is occupied by  $n_i$  particles, and thus the total number of particles and the total energy are

$$N' = \sum_i n_i, \quad E_k = \sum_i \epsilon_i n_i.$$

The partition function of Eq. (1.1) becomes easy to compute, yielding

$$\begin{aligned}\mathcal{Z}(\beta, \mu) &= \sum_{n_0=0}^{\infty} \sum_{n_1=0}^{\infty} \dots e^{\beta\mu \sum_i n_i} e^{-\beta \sum_i \epsilon_i n_i} = \left( \sum_{n_0} e^{\beta\mu n_0} e^{-\beta\epsilon_0 n_0} \right) \left( \sum_{n_1} e^{\beta\mu n_1} e^{-\beta\epsilon_1 n_1} \right) = \\ &= \prod_i \sum_{n_i} \left[ e^{\beta(\mu - \epsilon_i)} \right]^{n_i} = \prod_i \frac{1}{1 - e^{\beta(\mu - \epsilon_i)}}.\end{aligned}$$

Note that the condition  $\mu < \epsilon_0$  must be satisfied for the convergence of the series. It is interesting to study the total number of particles, which can be obtained from the potential of Eq. (1.2):

$$N = \langle N' \rangle = -\frac{\partial \Omega}{\partial \mu} = k_B T \frac{\partial \log \mathcal{Z}}{\partial \mu} = \sum_i \frac{1}{e^{\beta(\epsilon_i - \mu)} - 1} = \sum_i \langle n_i \rangle,$$

hence revealing the famous *Bose-Einstein distribution*

$$\langle n_i \rangle = \frac{1}{e^{\beta(\epsilon_i - \mu)} - 1}.$$

The occupation number of the ground state is  $N_0 = \langle n_0 \rangle$  and the remaining particles are called the thermal component  $N_T = N - N_0$ .

The origin of the Bose-Einstein condensation phenomenon is that  $N_0 \rightarrow \infty$  when  $\mu \rightarrow \epsilon_0$ . In particular, at a fixed temperature  $T$ , the function  $N_T(\mu)$  has a maximum  $N_c$  at  $\mu = \epsilon_0$ , while  $N_0$  is divergent. This implies that:

- if  $N_c > N$ , then the normalization condition  $N = N_0 + N_T$  is satisfied for values of  $\mu < \epsilon_0$  and  $N_0$  is negligible (no condensation);
- if  $N_c = N$ , it means that we are at the critical temperature  $T_c$  defined by  $N_T(T = T_c, \mu = \epsilon_0) = N$ . Since  $N_T$  is an increasing function of  $T$ , the previous scenario corresponds to  $T > T_c$ ;
- if  $N_c < N$  (or  $T < T_c$ ), the contribution of  $N_0$  is crucial for the normalization and thus the condensation happens.

In a finite box of volume  $V$ , where the lowest energy eigenvalue is  $\epsilon_0 = 0$ , the condensate fraction for  $T < T_c$  is expressed by

$$\frac{N_0}{N} = 1 - \left( \frac{T}{T_c} \right)^{3/2}.$$

Since  $N_0 \approx 0$  for  $T > T_c$ , the function has a discontinuity of its derivative at the critical temperature: a typical symptom of phase transitions.

The behavior is similar for a system trapped in an external harmonic potential, where the condensate fraction is

$$\frac{N_0}{N} = 1 - \left( \frac{T}{T_c} \right)^3$$

and the critical temperature depends on the oscillation frequencies.

## 1.2 Gross-Pitaevskii equation

For a 1D single-component BEC, namely made of only one species of  $N$  indistinguishable bosons, one can use a single wavefunction  $\psi(x, t)$  to describe its ground state by exploiting a mean-field approximation, thus revealing the Gross-Pitaevskii equation (GPE):

$$i\hbar \frac{\partial \psi(x, t)}{\partial t} = \left[ -\frac{\hbar^2}{2m} \nabla^2 + V(x, t) + g|\psi(x, t)|^2 \right] \psi(x, t). \quad (1.3)$$

The unusual term in this equation is the one proportional to the square modulus of the wavefunction through the constant  $g$ , called the *contact interaction constant*, that describes the interactions between bosons. In fact, for an ideal gas of non-interacting bosons,  $g = 0$  and one retrieves the standard Schrödinger equation. The interaction constant can be written in terms of the boson-boson scattering length  $a$ , a typical property of elastic collisions, by

$$g = \frac{4\pi\hbar^2}{m} a,$$

with  $g > 0$  for a stable BEC (for  $g < 0$  the system is unstable and collapses on itself).

The GPE can be written in its stationary form as

$$\left[ -\frac{\hbar^2}{2m} \nabla^2 + V(x) + g|\psi(x)|^2 \right] \psi(x) = \mu\psi(x), \quad (1.4)$$

where  $\mu \approx \frac{\partial E}{\partial N}$  is the chemical potential and accounts for the energy contribution of a single particle. Spatial properties of the condensate can arise from this equation, especially in the case of  $N \gg 1$  and when the interaction term is dominating on the kinetic energy term. By neglecting the kinetic term from Eq. (1.4), one easily gets the stationary solution

$$|\psi(x)|^2 = n(x) = \frac{\mu - V(x)}{g},$$

where  $n(x)$  is the density distribution, and the association of the latter with the square modulus of the wavefunction leads to the normalization condition  $\int |\psi(x)|^2 dx = N$ . A relevant case is when the external potential is harmonic, yielding a parabolic distribution

$$n(x) = \frac{\mu - \frac{1}{2}m\omega^2x^2}{g} = 0 \quad \Leftrightarrow \quad x = R_{\text{TF}} = \sqrt{\frac{2\mu}{m\omega^2}}, \quad (1.5)$$

with  $R_{\text{TF}}$  being the Thomas-Fermi radius, a parameter indicating the spatial confinement of the condensate.

## 1.3 Two-component mixture

When the system is composed of two different species ( $a$  and  $b$ ), Eq. (1.4) splits into two coupled stationary GPEs:

$$\begin{aligned} \left[ -\frac{\hbar^2}{2m_a} \nabla^2 + V(x) + g_{aa}|\psi_a(x)|^2 + g_{ab}|\psi_b(x)|^2 \right] \psi_a(x) &= \mu_a \psi_a(x), \\ \left[ -\frac{\hbar^2}{2m_b} \nabla^2 + V(x) + g_{ab}|\psi_a(x)|^2 + g_{bb}|\psi_b(x)|^2 \right] \psi_b(x) &= \mu_b \psi_b(x). \end{aligned} \quad (1.6)$$

This is due to the possibility of collisions not only between bosons  $a$ - $a$  or  $b$ - $b$ , but also of the type  $a$ - $b$ , thus producing three interaction constants  $g_{aa}, g_{bb}, g_{ab}$ . Depending on those constants' values, the system can assume different behaviors and ground state configurations.

For example, take the case of a flat box potential in a total fixed volume  $V$ , yielding constant densities. Letting  $n_a = |\psi_a|^2$  and  $n_b = |\psi_b|^2$ , we can express the energy density in the following way:

$$\mathcal{E} = \frac{1}{2}g_a n_a^2 + \frac{1}{2}g_b n_b^2 + g_{ab}n_a n_b - \mu_a n_a - \mu_b n_b,$$

where the first three terms represent the interactions between particles of the same type and between different ones, while the last two terms account for the chemical potentials. Now, we state that the system is thermodynamically stable and miscible if and only if the Hessian of  $\mathcal{E}$  with respect to  $n_a$  and  $n_b$  is positive-definite. The calculation is straight-forward:

$$H = \begin{bmatrix} \frac{\partial^2 \mathcal{E}}{\partial n_a^2} & \frac{\partial^2 \mathcal{E}}{\partial n_a \partial n_b} \\ \frac{\partial^2 \mathcal{E}}{\partial n_a \partial n_b} & \frac{\partial^2 \mathcal{E}}{\partial n_b^2} \end{bmatrix} = \begin{bmatrix} g_a & g_{ab} \\ g_{ab} & g_b \end{bmatrix} > 0 \quad \Leftrightarrow \quad \begin{cases} g_a > 0 \\ g_b > 0 \\ g_a g_b > g_{ab}^2 \end{cases}.$$

The first two conditions ensure that neither  $a$  nor  $b$  collapse, while the latter expresses the condition for miscibility. Intuitively, if  $g_{ab}$  is small with respect to the other constants, it means that the two species do not interact much one with the other, thus letting themselves mix and spatially overlap. On the other hand, if  $g_{ab}$  is big (and positive), they strongly repulse and undergo a phase separation. From now on, only repulsive interactions will be considered, so the only possibilities will be immiscible or miscible (no collapse).

In the more general case of a non-uniform trapping potential, the densities depend from the position and the distributions are correlated with the interaction constants. Considering the harmonic trap and the miscible case, if  $g_a > g_b$  then the species  $b$  will be confined in a small central region, while the species  $a$  will occupy more space. This is shown in the lower section of

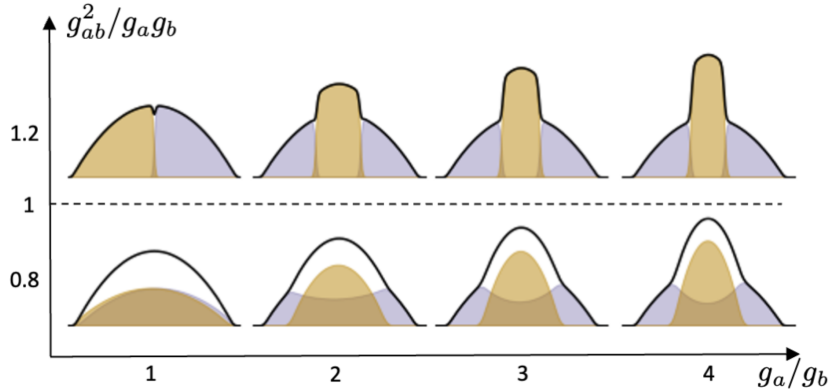


Figure 1.1: GPE simulation of a two-component balanced mixture in a harmonic potential. The shaded purple region shows the density distribution of population  $a$  and the yellow one the population  $b$ . Here, a small magnetic field is used to break the left-right symmetry. The total density profile is drawn in black. *From Ref. [5].*

Fig. 1.1, while the upper section shows the immiscible case and the buoyancy (again,  $g_a > g_b$ ). One notes that the total density profile is not Thomas-Fermi anymore when  $g_a \neq g_b$ .

## 1.4 Coherently coupled mixture

When the system is composed of two species of the same atom, such as two hyperfine states, the dynamics become more interesting because of the possible interconversion processes. One possibility is to use a homogeneous microwave radiation, which couples by a Rabi process (i.e. single-photon exchange) the two internal states  $|a\rangle$  and  $|b\rangle$ . The time-dependent field of the radiation is of the type

$$\Omega_R(t) \exp\left\{-i\omega_{\text{cpl}}t + \phi\right\}, \quad \text{with } \omega_{\text{cpl}} = \omega_{ab} + \delta_B.$$

Here,  $\omega_{ab}$  is the transition frequency between the two coupled states, and in the case of two hyperfine states of the same angular momentum level it includes the linear Zeeman splitting of a small external magnetic field. The coupling frequency  $\omega_{\text{cpl}}$  differs from  $\omega_{ab}$  by a parameter  $\delta_B$  called *detuning*.

In this setting, the two-component GPEs of Eq. (1.6) become coupled in the following way:

$$\begin{aligned} \left[ -\frac{\hbar^2}{2m} \nabla^2 + V(x) - \frac{\delta_B}{2} + g_{aa}|\psi_a(x)|^2 + g_{ab}|\psi_b(x)|^2 \right] \psi_a(x) - \frac{\hbar\Omega_R}{2} \psi_b(x) &= \mu_a \psi_a(x), \\ \left[ -\frac{\hbar^2}{2m} \nabla^2 + V(x) + \frac{\delta_B}{2} + g_{ab}|\psi_a(x)|^2 + g_{bb}|\psi_b(x)|^2 \right] \psi_b(x) - \frac{\hbar\Omega_R}{2} \psi_a(x) &= \mu_b \psi_b(x). \end{aligned} \quad (1.7)$$

Thanks to this type of coupling, even an immiscible mixture can spatially overlap. In this context, the system can be studied by looking at two distinct energy channels separately, namely the spin  $n_a - n_b$  and the total density  $n_a + n_b$ . The behavior of the spin channel is of great interest, because it shows magnetic properties, which are what we will focus on.

In this coupling regime, the wavefunction spatial changes of the condensate have characteristic lengths related to the spin/density channel and the coupling radiation, called *healing lengths*, which are the following:

$$\xi_s = \frac{\hbar}{\sqrt{2mn\delta g}}, \quad \xi_d = \frac{\hbar}{\sqrt{2m\bar{g}}}, \quad \xi_R = \sqrt{\frac{\hbar}{m\Omega_R}}, \quad (1.8)$$

where  $\bar{g} = (g_{aa} + g_{bb})/2$  and  $\delta g = \bar{g} - g_{ab}$ .

### 1.4.1 Ferromagnetism

The magnetic model of the system is shown in the phase diagram of Fig. 1.2, where a phase transition from *paramagnetism* to *ferromagnetism* occurs. Similarly to the miscible-immiscible phase transition, here the order parameter takes into account the interaction constants, but with the addition of the coupling radiation, and it is the ratio  $|\delta g|n/\hbar\Omega_R$ , where from now on  $n = n(x=0)$ .

The mean-field energy landscape of the system spin channel is given by the asymmetric double well

$$E_{\text{MF}}(Z) = -\hbar \left( |\delta g|nZ^2 + 2\Omega_R \sqrt{1 - Z^2} + 2\delta_{\text{eff}}Z \right), \quad (1.9)$$

where the coupling strength  $\Omega_R$  plays the role of the height of the barrier between the wells and the effective detuning  $\delta_{\text{eff}} = \delta_B + n(g_{aa} - g_{bb})$  contributes to the asymmetry of the wells. Depending on those values, different behaviors may occur. One may set a fixed value for  $\Omega_R$  and then probe the magnetic properties by changing  $\delta_{\text{eff}}$ .

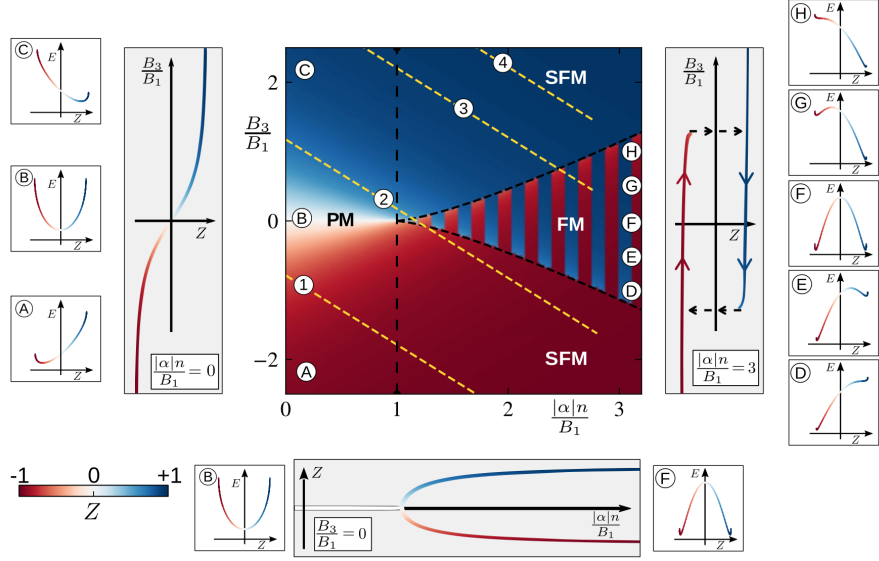


Figure 1.2: Phase diagram of the magnetic properties of the system, showing the magnetization of the ground state. The association between the diagram labels and the system quantities is  $\alpha \rightarrow \delta g$ ,  $B_3 \rightarrow \delta_{\text{eff}}$  and  $B_1 \rightarrow \Omega_R$ . When  $|\delta g|n < \hbar\Omega_R$  we are in the paramagnetic (PM) region. On the contrary, when  $|\delta g|n > \hbar\Omega_R$  the system can be either in the saturated ferromagnetic (SFM) region if  $\delta_{\text{eff}}$  is large enough or in the ferromagnetic (FM) region. *From Ref. [1]*

**Paramagnetism** In the case of  $|\delta g|n < \hbar\Omega_R$ , the energy landscape reduces to a single well and thus the system exhibits paramagnetic properties. The magnetization of the ground state changes continuously from  $Z = -1$  to  $Z = 1$  and does not depend on the history of the system.

**Ferromagnetism** On the other hand, when  $|\delta g|n > \hbar\Omega_R$  and  $|\delta_{\text{eff}}| < \delta_{\text{crit}}$  (to avoid being in the saturated ferromagnetic region),<sup>1</sup> the double well creates a metastable state, which can be the ground state depending on the history of the system, yielding an hysteresis cycle and a ferromagnetic behavior. This will lead directly to the phenomenon of domain walls and bubble formation analyzed in the following section.

## 1.5 False vacuum decay and bubble formation

False vacuum decay (FVD) is the process of transition between the metastable state and the true ground state of the system (as the lowest in energy). In the context of a many-body quantum system, this process can be treated using a field-theoretic approach, where the condensate is described by a macroscopic wavefunction. This allows us to capture the collective behavior of the particles and the dynamics of the phase transition. To understand the underlying mechanisms and dynamics of this process, let us delve into the reasons and methods by which it occurs.

Given the asymmetric double well describing the spin channel mean-field energy landscape of the condensate in the ferromagnetic region (schematic representation in Fig. 1.3), the metastable state A in which all atoms are in the state  $|\uparrow\rangle$  is called false vacuum (FV), since it

<sup>1</sup>As for the paramagnetic case, in the saturated ferromagnetic the energy landscape has only one minimum.

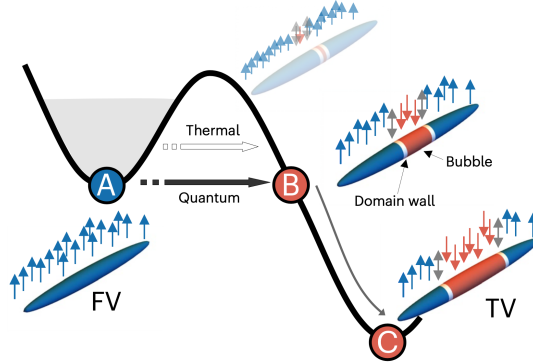


Figure 1.3: Ferromagnetic energy landscape and false vacuum decay via bubble formation. *From Ref. [7].*

is not the true ground state. The preparation of the system in this state, as shown in Fig. 1.4 is not trivial. At first, one has to set  $\Omega_R$  to a fixed value and  $\delta_{\text{eff}} > 0$  such that the system is in

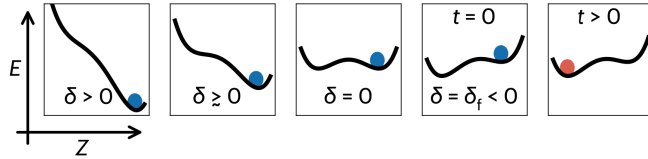


Figure 1.4: Preparation of the system in the metastable FV state by changing the detuning from a positive to a negative value until the energy configuration is the one of Fig. 1.3 at  $t = 0$ . After a waiting time  $t > 0$ , the system decays into the TV state. *From Ref. [7].*

the saturated ferromagnetic region and the ground state is at positive magnetization. Then, by lowering  $\delta_{\text{eff}}$ , the asymmetry can be shifted until the system is in the metastable state (one must not go beyond  $\delta_{\text{eff}} = \delta_{\text{crit}}$  because it would return to the saturated region).

The possibility of tunnelling to the state B arises from the fact that the bubble formation has an energy cost due to the kinetic contribution of the interaction on the interface (domain wall) between atoms  $|\uparrow\rangle$  and  $|\downarrow\rangle$ . However, when a sufficient number of atoms in the core region flips to  $|\downarrow\rangle$ , the energy gain compensates the kinetic cost and the tunnelling can occur resonantly from A to B.<sup>2</sup> Once happened, the system is not in a metastable state anymore, hence the decaying into the ground state C, the true vacuum (TV), via bubble expansion with more atoms flipping into the  $|\downarrow\rangle$  state. Note that the TV is not composed of all atoms  $|\downarrow\rangle$ . This is because while the  $|\downarrow\rangle$  state is energetically lower in the high-density core region, the situation is opposite in the low-density tails, due to the dependence of the effective detuning on the density.

From an experimental point of view, the parameters to vary are  $\Omega_R$  and  $\delta_{\text{eff}}$ , that contribute to the energy landscape and hence to the decay process. We expect FVD to be greatly influenced by the depth of the well (the energy difference between FV and TV), and thus by both parameters, since it tells us how much energy the system has to dissipate.

Another important factor to focus on is time. The reason is that the tunnelling through the

<sup>2</sup>Pure quantum tunnelling occurs at  $T = 0$ . At non-zero temperature the process is helped by thermal excitations.

## CHAPTER 1. THEORETICAL BACKGROUND

energy barrier is a stochastic process and does not happen at a fixed time. The problem arises when one is willing to study the bubble evolution during the decay. After the condensate is prepared in the metastable state, we can wait for an interval of time  $\Delta t$  and then decide to look at the system, but due to its quantum nature, a measure will destroy our information, and we will not be able to let it evolve. The system will have to be prepared again in the initial state and so on. By recreating the experiment many times, changing the experimental waiting time, one should get a fair picture of the bubble evolution, but relying on time only may not be enough. Since we know the bubble expands, it will be useful to look at its size,  $\sigma_B$ , as an evolution parameter.

# Chapter 2

## Data analysis

In this chapter we describe the experimental platform in which the measurements were carried out and we then proceed with the characterization of the false vacuum decay bubbles through data analysis. Data is taken from the measurements done for the FVD experiment of Ref. [7]. Our aim is to study the magnetization properties of the system in the bubble (*inside* region), around its *domain walls* and also in the *outside* region, as sketched in Fig. 2.1. We are looking

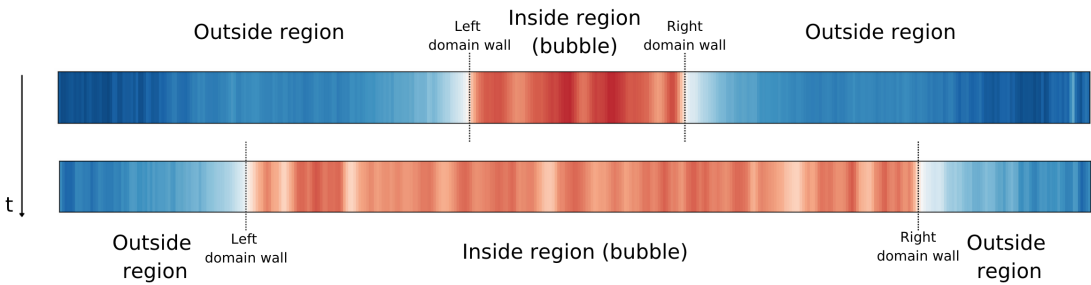


Figure 2.1: Separation of the system into inside and outside region by left and right domain walls for two example bubbles. The lower bubble is measured after a higher waiting time  $t$  and it has a bigger size.

for correlations between the external parameters  $\Omega_R$  and  $\delta_{\text{eff}}$ , and the bubble properties such as its size  $\sigma_B$ , its domain wall width  $w_D$  and the experimental waiting time  $t$ . It is also possible to notice some periodic structures in the system, both inside and outside. Then, for a spectral analysis, FFT and ACF will be utilized.

The code for the analysis was written in the **Python** programming language. The references used in this chapter are mainly [1], [4], [2] and [3].

### 2.1 Experimental platform

The experimental platform is composed of a bosonic gas of  $N \sim 10^6$   $^{23}\text{Na}$  atoms, optically trapped and cooled below the condensation temperature, with typical peak densities of  $n = 10^{14}$  atoms/cm<sup>3</sup>. The initial spin state in which the system is prepared is  $|F, m_F\rangle = |2, -2\rangle = |\uparrow\rangle$ ,

with  $F$  being the total angular momentum of the atom and  $m_F$  its projection on the quantization axis. The  $|\uparrow\rangle$  state is then coupled to  $|1, -1\rangle = |\downarrow\rangle$  through microwave radiation with amplitude  $\Omega_R$ . The relevant scattering lengths concerning the two states are  $a_{\uparrow} = 64.3a_0$ ,  $a_{\downarrow} = 54.5a_0$  and  $a_{\uparrow\downarrow} = 64.3a_0$ .

The trapping potential is harmonic in all three directions, but strongly asymmetric concerning the radial ( $\rho$ ) and axial ( $x$ ) directions. In fact, the trapping frequencies are respectively  $\omega_{\rho}/2\pi = 2$  kHz and  $\omega_x/2\pi = 20$  Hz, yielding an elongated system (cigar-shaped) with inhomogeneous density. The spatial size of the system is given by the Thomas-Fermi radii  $R_{\rho} = 2$  μm and  $R_x = 200$  μm, calculated with Eq. (1.5). This particular setup is helpful for suppressing the radial spin dynamics of the condensate and thus reducing it from a 3D system of density  $n_{3D}(r_{\perp}, x)$  to a 1D system of linear density  $n(x)$ , with the only difference being the renormalization of the  $\delta g$  parameter that appears in Eq. (1.9):

$$\delta g \rightarrow k = \frac{2}{3} \frac{n_{3D}}{n} \delta g.$$

In order to extract the density distribution, the two spin states are treated independently one from another, and a spin-selective imaging process is performed. Then, an integration along the transverse direction is carried out, obtaining two 1D density profiles  $n_{\uparrow}(x)$  for the atoms in the state  $|\uparrow\rangle$  and  $n_{\downarrow}(x)$  for the atoms in the state  $|\downarrow\rangle$ , from which one can extract the relative magnetization

$$Z(x) = \frac{n_{\uparrow}(x) - n_{\downarrow}(x)}{n_{\uparrow}(x) + n_{\downarrow}(x)}. \quad (2.1)$$

## 2.2 Raw data

Raw data is organized in a hierarchical system. At a fixed instant, the condensate's measured data are called a *shot* (it refers to the imaging process). Each shot is part of a series of them that can be analyzed as the time evolution of a single system: this series is called a *sequence*. Eventually, during a *day* of measurements, many sequences may be collected, and a selection of them will be studied in the following analysis. For each sequence, the experimental data contains also the radiation coupling  $\Omega_R$  in a range between  $2\pi \times 200$  Hz and  $2\pi \times 800$  Hz (it changes from one day of measurements to another) and the detuning  $\delta_{\text{eff}}$  in a range between  $2\pi \times 100$  Hz and  $2\pi \times 600$  Hz. For each shot, the experimental waiting time  $t$  provides information on the time interval passed before the imaging process, ranging from 1 ms to 300 ms.

A shot contains all the information on the system after waiting for a time  $t$ , including the two population densities,  $n_{\uparrow}(x)$  and  $n_{\downarrow}(x)$ , distributed on a length scale from 0 to 400 pixels. The spatial resolution of the image is 1 pixel = 1.025 μm ≈ 1 μm, so the two length units will often be used interchangeably. The magnetization data  $Z(x)$  is calculated with Eq. (2.1) and, by definition, composed of a series of values ranging from  $-1$  (all atoms in the state  $|\downarrow\rangle$ ) to  $1$  (all atoms in the state  $|\uparrow\rangle$ ).

Since our focus is to characterize the bubble properties, first we need to extract the spatial parameters of the bubble in order to locate it in each shot, then we will proceed with the study of its evolution.

### 2.2.1 Bubble fit parameters

In order to localize the bubble in a shot, the most interesting parameters to retrieve are the bubble center  $x_0$  and its width  $\sigma_B$ . However, not all shots contain a bubble, namely the ones

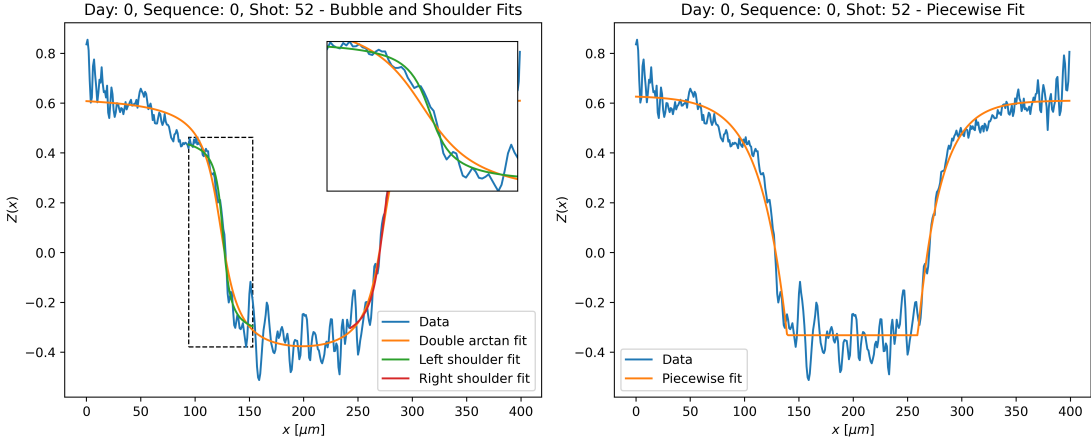


Figure 2.2: Example of fit results performed on a shot. First, the data is fitted with the double-arc tangent function of Eq. (2.2), then each domain wall is fitted with a single-arc tangent, namely the one of Eq. (2.3). This ensures a better estimation of the domain wall centers and thus of the bubble width. Eventually, a last fit is done with the piecewise function of Eq. (2.4), in order to capture the inside/outside discontinuity and the exponential tails.

taken when the bubble was not formed yet. We can easily classify the two types of shots by computing the magnetization average in the central region and using a threshold value, set to  $Z_{\text{thr}} = -0.2$ .

To parametrize the bubble, the magnetization data is fitted with a double-arc tangent function

$$Z_{\text{fit}}(x) = -A \left[ \frac{2}{\pi} \arctan\left(\frac{x - c_1}{w_1}\right) - \frac{2}{\pi} \arctan\left(\frac{x - c_2}{w_2}\right) \right] + \Delta, \quad (2.2)$$

where  $c_1$  and  $c_2$  are the centers' positions of the arc tangent "shoulders", corresponding to the domain walls, and  $w_1$  and  $w_2$  are their characteristic widths. Then, for a better result, a further fit is performed on each domain wall with a single-arc tangent function

$$Z_{\text{fit}}(x) = -A \frac{2}{\pi} \arctan\left(\frac{x - c_{1,2}}{w_{1,2}}\right) + \Delta, \quad (2.3)$$

yielding the domain wall center position  $c_{1,2}$ . Eventually, we obtain the bubble center position  $x_0 = (c_1 + c_2)/2$  and the bubble width  $\sigma_B = c_2 - c_1$ .

While this routine is very accurate for determining the domain wall profile and hence the bubble width, it may be useful to try fitting the data to another function, such as

$$Z_{\text{fit}}(x) = \begin{cases} (A - \Delta_1) \exp\left(\frac{x - x_1}{w_1}\right) + \Delta_1 & \text{for } x < x_1 \\ A & \text{for } x_1 < x < x_2, \\ (A - \Delta_2) \exp\left(-\frac{x - x_2}{w_2}\right) + \Delta_2 & \text{for } x > x_2 \end{cases}, \quad (2.4)$$

which is made of two exponentials and a constant value in the middle. As it turns out, this approach ensures a better estimation of the inside region, whose limits are  $x_1$  and  $x_2$ . The exponential tails give also a characteristic width for the domain wall region, namely  $w_D = (w_1 + w_2)/2$ .

An example of fitting with the arctangent and stepwise exponential functions is provided in Fig. 2.2.

### 2.2.2 Shot sorting

Once the bubble width  $\sigma_B$  is retrieved, it is useful to order the shots in a sequence by this parameter. This process lets us display the system evolution, in contrast to the original shot ordering based on the experimental time waited before observing the bubble. The reason why we are more interested in the size dependence is that the bubble formation event is a stochastic process (the tunneling through the energy barrier), and the time at which a bubble forms is not determined. However, theory suggests that once the bubble is formed, its evolution (the decay from FV to TV) is determined. An example of sorting by both time and size is shown in Fig. 2.3 with a colormap displaying the magnetization profiles (blue is for positive Z and red for negative Z).

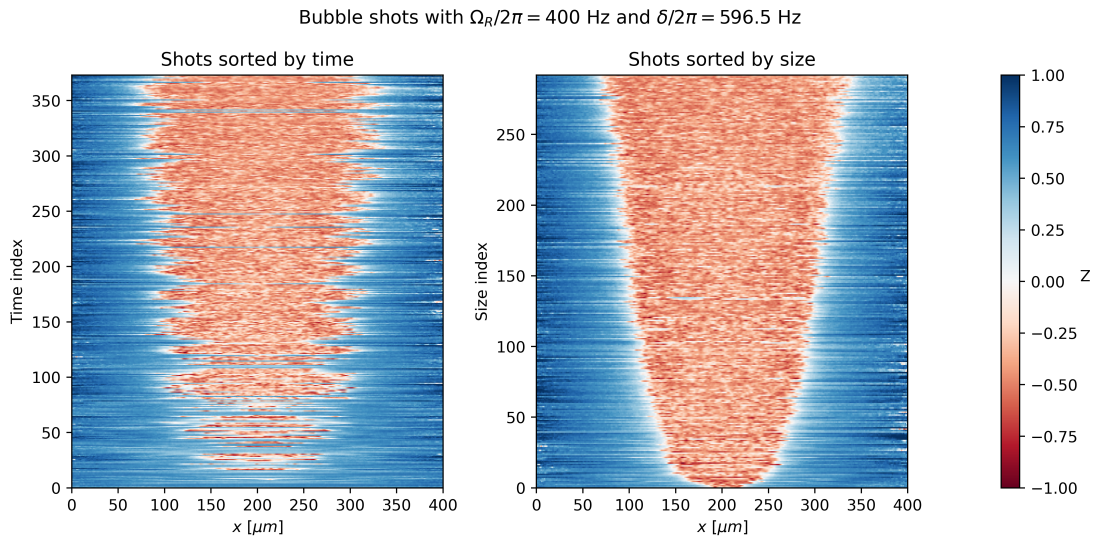


Figure 2.3: Example of initial shot sorting based on experimental waiting time (on the left) and final sorting based on bubble width  $\sigma_B$  (on the right) for all shots with  $\Omega_R/2\pi = 400$  Hz and  $\delta_{\text{eff}}/2\pi = -596.5$  Hz. The  $\sigma_B$  parameter is estimated from the previous fitting procedure, and the no-bubble shots ( $\sigma_B = 0$ ) are removed from the right plot. The data is colored by mapping positive magnetization to blue and negative magnetization to red.

## 2.3 Parameters analysis

In order to look at the distribution of the bubble parameters versus the experimental time or the bubble size, we decide to group all shots by the radiation coupling  $\Omega_R$  (ignoring the detuning  $\delta_{\text{eff}}$ ) and plot the bubble width  $\sigma_B$  and domain wall width  $w_D$ .

An approach to this might be the one of ordering the shots by time or size and then dividing all shots in blocks with a fixed number of shots per block. However, the distributions of  $t$  and  $\sigma_B$  are not continuous (especially  $t$ , which is discretized), and it may be convenient to look for clustered data. The clustering approach can be implemented by the **K-Means** algorithm from

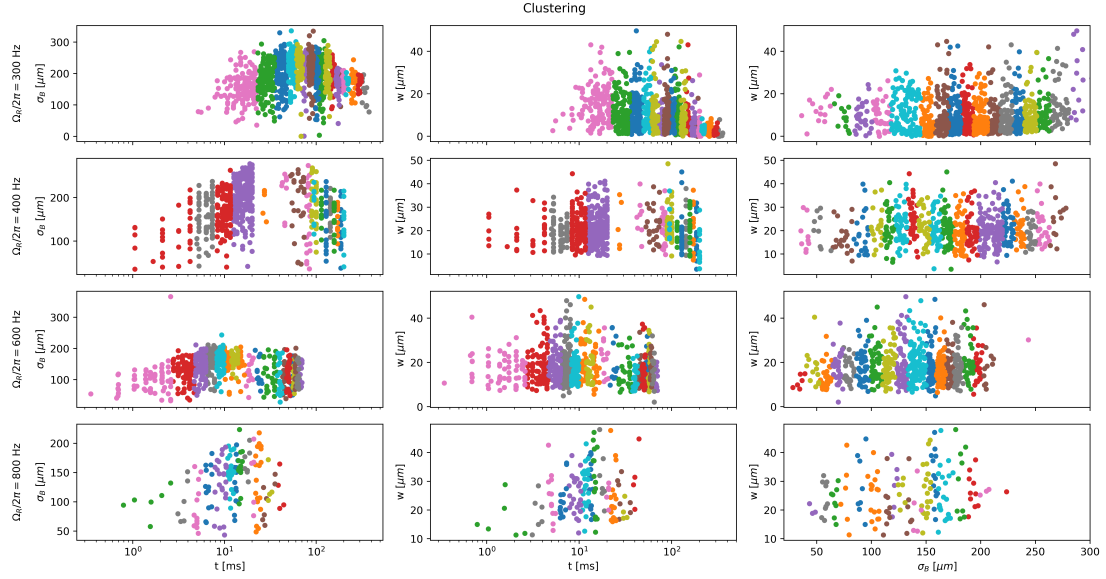


Figure 2.4: Data clustering with the K-Means algorithm and  $n_{\text{clusters}} = 20$  based only on  $t$  (first two columns from the left) or  $\sigma_B$  (third column). The first column shows the  $\sigma_B$  data on the y-axis, while the last two show the  $w_D$  data.

the **Scikit-Learn** Python library, which lets us choose the number of clusters. The clustered data, with  $n_{\text{clusters}} = 20$ , is shown in Fig. 2.4.

The bubble parameters, averaged in each cluster and in relation one to another, are shown in Fig. 2.5. The domain wall width does not show any visible pattern when varying the bubble size, and for this reason it is averaged and shown as a function of  $\Omega_R/2\pi$  in the upper right plot, where it increases with  $\Omega_R$  although the points at 400 Hz and 600 Hz interrupt the monotony. The behavior against time is slightly increasing for small time and decreasing for long times, but the most significant trend is clearly the one of  $\sigma_B$  vs  $t$ , where the bubble size is increasing with time at first, and then decreases. The initial behavior corresponds to the power-law growth of  $\sigma_B$  in time of the type

$$\sigma_B(t) = A \left( \frac{t}{1 \text{ ms}} \right)^B,$$

the final one is probability an artifact due to the low-density tails of the Thomas-Fermi distribution. Eventually, a linear fit is performed on the log-log data with the aim of finding the power-law coefficient  $B$  for each value of the radiation coupling, shown in the lower right corner of Fig. 2.5. The values are all compatible among them, hence revealing that the bubble grows with the same profile at different values of  $\Omega_R$ .

## 2.4 Spectral analysis

Since we are interested in the properties of the bubble throughout its evolution, periodic signals in the magnetization channel and their relation to the waiting time or the bubble size are important features to focus on. In order to study them, a spectral profile is much needed, from

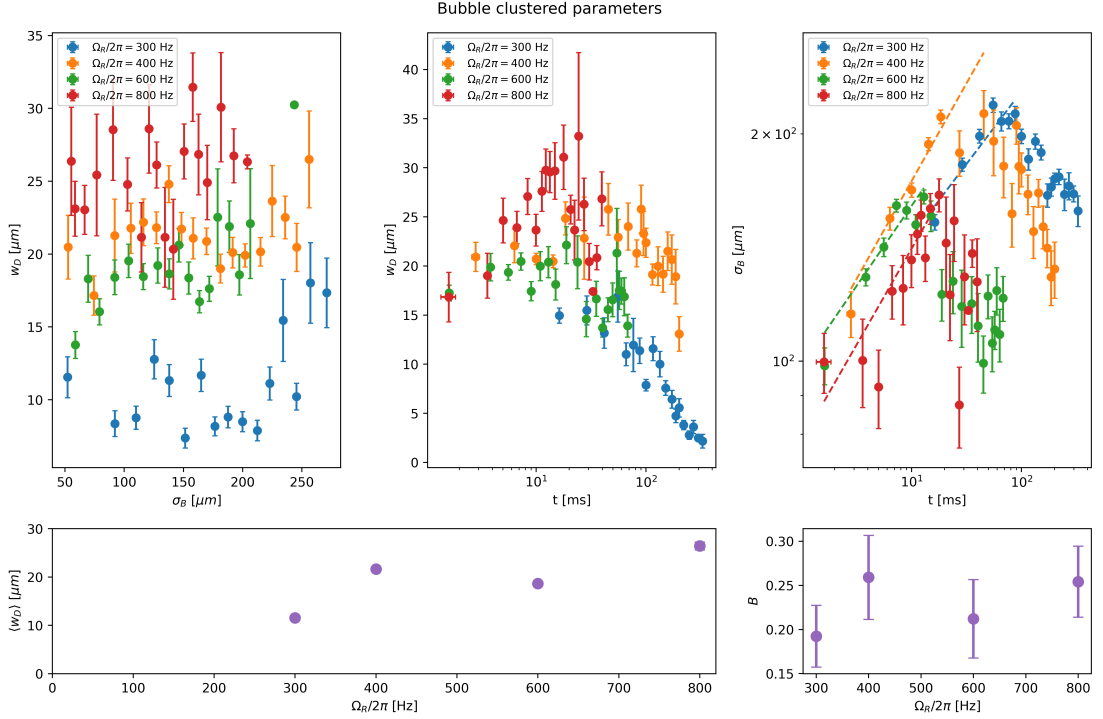


Figure 2.5: Bubble parameters distribution averaged on all shots of the same cluster. The upper panel shows, from left to right,  $w_D$  vs  $\sigma_B$ ,  $w_D$  vs  $t$  and  $\sigma_B$  vs  $t$  (the last one in log-log scale). Errors are estimated with the standard deviation of the values in the cluster. The lower panel presents on the left the average domain wall width over all shots with the same coupling radiation  $\Omega_R$ . A linear fit on the log-log increasing data is performed in order to estimate the rate of growth, shown on the right of the bottom panel.

which one can extrapolate the main frequencies of the signals and, most importantly, the typical length scales of the system. Finding a characteristic frequency/length inside or outside the bubble could help to understand how the system dissipates energy in the decay.

The tools used in the following analysis are the Fast Fourier Transform (FFT) and the auto-correlation function (ACF).

### 2.4.1 FFT and ACF definition

**FFT** We will first approach the problem of deriving such a profile by using the Fast Fourier Transform (FFT), an algorithm that implements the Discrete Fourier Transform (DFT) in an efficient manner.<sup>1</sup> Given the input as a sequence of  $N$  discrete values  $Z_0, \dots, Z_{N-1}$  sampled with spacing  $\Delta x$ , by definition the DFT is a series of  $N$  discrete values  $\mathcal{F}_0, \dots, \mathcal{F}_{N-1}$  spaced by

<sup>1</sup>There are several efficient methods to compute the DFT. The most common implementation is the Cooley-Tukey algorithm, used in the **Scipy** Python library for FFT.

$\Delta k = 1/(N\Delta x)$  and convoluted with a complex phase such that

$$\mathcal{F}_k = \sum_{n=0}^{N-1} Z_n e^{-2\pi i \frac{k}{N} n}.$$

When the input  $Z_n$  is real-valued, the transform is too, and it is also symmetric between positive and negative frequencies. We neglect unphysical negative frequencies by using the Scipy function `rfft` instead of `fft`.

The result of the Fourier transform of a signal is the extraction of the main frequency components of the signal itself. In fact, as we know, the transform of a pure sinusoidal signal with frequency  $\omega_0$  results in a Dirac delta at  $\omega = \omega_0$  (excluding the negative frequencies). In the general case of a signal made up of more frequency components and with noise, the peaks in the Fourier transform will correspond to the most relevant frequencies. Note that in our case the signal is in the space-domain, and by taking the inverse of the points in the frequency-domain, one can get information about the spatial periodicity of the system, hence the typical length scale.

**ACF** Another tool that can be used to study the periodic properties of a signal is the autocorrelation function (ACF). Similarly to the DFT, the ACF is also a particular type of convolution, where the signal is convoluted with itself. The caveat here is that since our signal is of finite length, the whole convolution would show boundary effects, as shown in Fig. 2.6. It is then

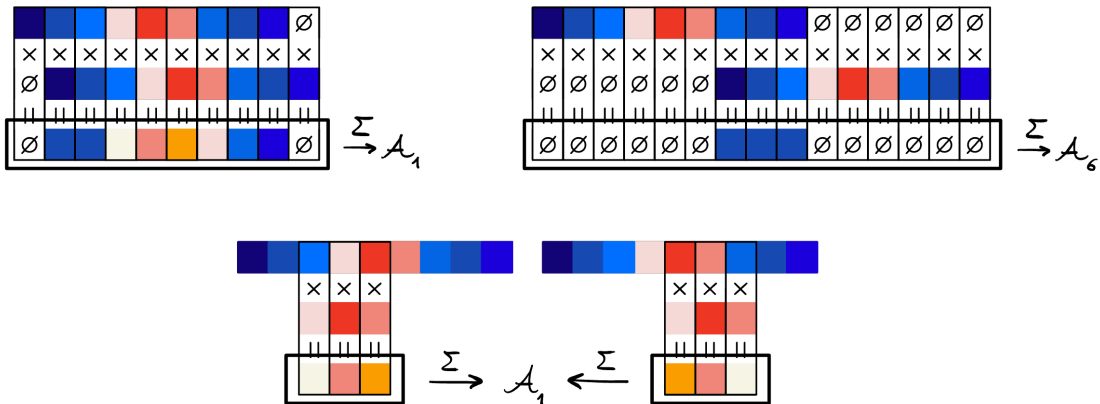


Figure 2.6: Schematic representation of ACF. Boundary effects arise when computing the autocorrelation function on the whole signal (top). Since the signal is finite, the contributions on the borders are set to zero. When restricting to windowed autocorrelation, no boundary effects are present anymore (bottom).

worth limiting the signal in a central window of length  $2W$  and computing the ACF on the windowed signal (Fig. 2.6). Taking as input the latter as  $Z_0, \dots, Z_{2W-1}$ , the output will be a series of values  $\mathcal{A}_0, \dots, \mathcal{A}_W$  living in the space-domain<sup>2</sup> such that:

$$\mathcal{A}_k = \frac{1}{2} \left( \frac{\sum_n Z_n Z_{n+k}}{\sqrt{\sum_n Z_n^2 \sum_n Z_{n+k}^2}} + \frac{\sum_n Z_n Z_{n-k}}{\sqrt{\sum_n Z_n^2 \sum_n Z_{n-k}^2}} \right).$$

<sup>2</sup>While the FFT domain is made of frequencies, the ACF domain is instead made of lag values, corresponding to the spatial shifts of the signal.

This formula computes the windowed autocorrelation by shifting the signal both to the left and to the right and then taking the average. Both terms are normalized in order to get  $\mathcal{A}_0 = 1$ . Note that the sums run from  $n = 0$  to  $n = W - 1$  and thus the length of the signal must be greater than  $4W$ : data that does not respect this condition will not be analyzed.

The computation of this function on a simple sinusoidal signal is shown in App. A. In contrast to the FFT, the ACF results, as mentioned before, live in the space-domain and give direct results on the length scales. A high ACF value at  $\Delta x_0$  means that the signal is correlated with itself when shifted by  $\Delta x_0$ . The periodicity of the signal is then related to the length  $\Delta x_0$ .

### 2.4.2 FFT and ACF analysis on sequences

Now, what we shall do is computing the FFT and the ACF on the data, taking care of the fact that it is necessary to separate the inside region (the bubble) from the outside one. This is done by relying on the piecewise exponential fit results, namely the positions  $x_1$  and  $x_2$  from Eq. (2.4). An example of the inside region analysis for a selected pair of values  $\Omega_R$ ,  $\delta_{\text{eff}}$  (the same of Fig.

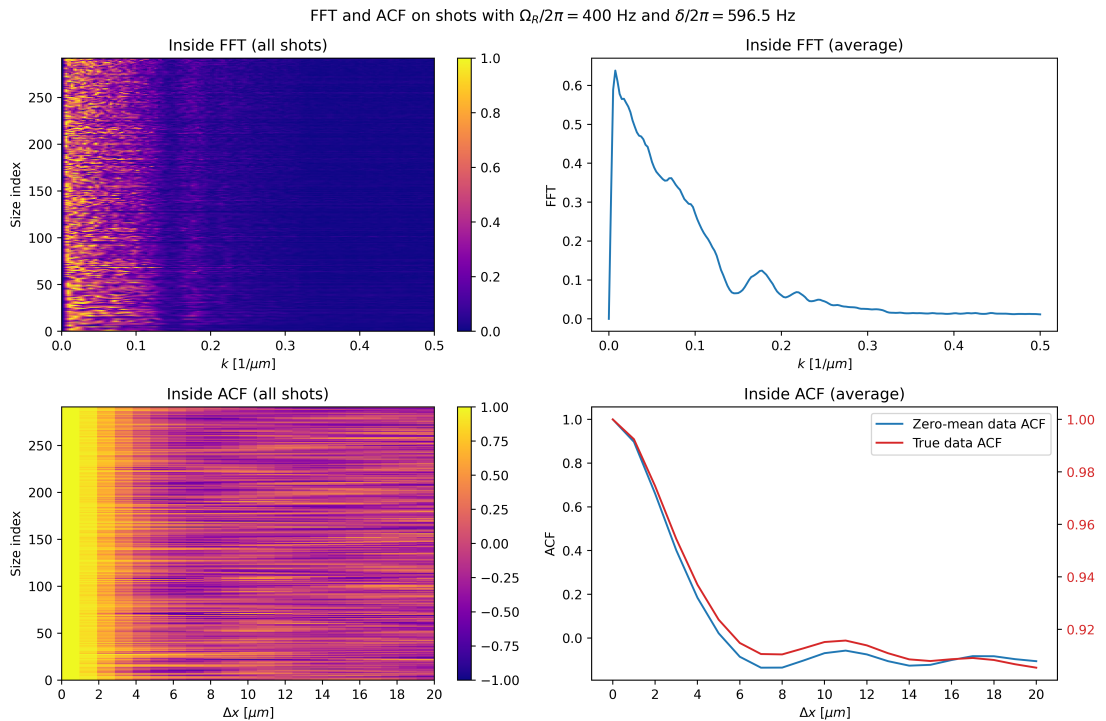


Figure 2.7: Example of FFT and ACF calculated on the inside region of shots with  $\Omega_R/2\pi = 400$  Hz and  $\delta_{\text{eff}}/2\pi = -596.5$  Hz, after selecting the shots where  $x_2 - x_1 > 4W = 80$   $\mu\text{m}$ . The values for each shot are shown in the left graphs with colormaps, while the averages on all shots are on the right. Note that before computing the transforms the data was set to zero-mean by subtracting its average. In the lower right graph, ACF computed on the true data (without the 0-mean) is shown for comparison to the other ACF profile.

2.3) is presented in Fig. 2.7, where the data was first set to zero-mean and only the shots where  $x_2 - x_1 > 4W$  are selected, with  $W = 20$   $\mu\text{m}$ .

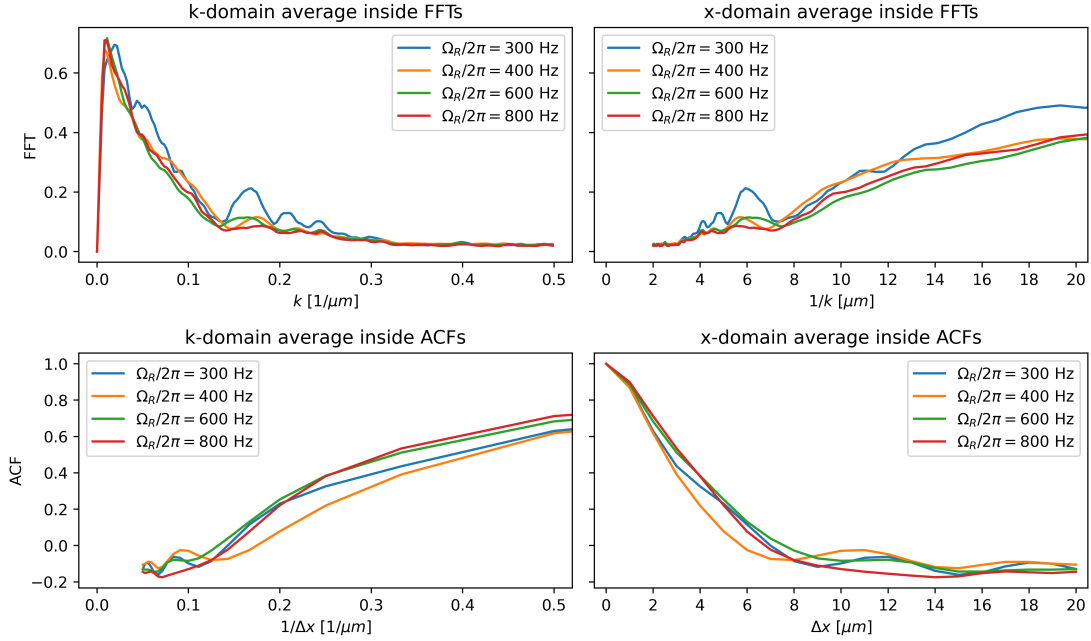


Figure 2.8: FFT and ACF profiles (computed with zero-mean data) averaged over all sequences with the same radiation coupling  $\Omega_R$ . On the top, the FFTs are plotted both in the  $k$ -domain and  $x$ -domain. On the bottom, the ACFs are also plotted in the two domains to match the upper panel and confront the results. The FFTs are peaked at  $k_{\text{FFT}} \sim 0.01 \mu\text{m}^{-1}$ , while the first ACF peaks are at  $\Delta x_{\text{ACF}} \sim 10 - 11 \mu\text{m}$ .

Let us briefly discuss the behaviors of the computed FFTs and ACFs, considering that it is similar for all  $\Omega_R$ ,  $\delta_{\text{eff}}$  and the example presented is a good one (see also Fig. 2.8, showing the profiles averaged over all sequences with the same  $\Omega_R$ ). The FFT shows a peak at a frequency in the order of  $k_{\text{FFT}} \sim 0.01 \mu\text{m}^{-1}$  and of width in the order of  $\Delta k_{\text{FFT}} \sim 0.1 \mu\text{m}^{-1}$ . The ACF instead has a first peak at  $\Delta x_{\text{ACF}} \sim 10 - 11 \mu\text{m}$ . By comparing these results and relying on the FFT and ACF definitions, the relation should be  $k = 1/\Delta x$ . However, by taking the inverse of the ACF peak values, one gets  $k_{\text{ACF}} \sim 0.1 \mu\text{m}^{-1}$ , a frequency hidden in the FFT plot due to the broad peak. The reason for the peak broadness is probability the data noise, which is difficult to analyze properly. We will thus proceed by relying only on the ACF for the remaining analysis.

### 2.4.3 ACF analysis on all shots

From now on, all shots will be considered, taking into account all  $\Omega_R$  and  $\delta_{\text{eff}}$  values. What we shall proceed to do is studying the ACF parameters as functions of the bubble properties  $t$  and  $\sigma_B$ , and of the experimental external parameters  $\Omega_R$  and  $\delta_{\text{eff}}$ . The routine is the following:

1. Gather all shots with the same  $\Omega_R$  and save their bubble parameters;
2. Select only the shots where the inside or outside region is at least  $4W$  pixels long;
3. Sort the shots based on the waiting time or the bubble size;

4. Cluster the shots based on the sorting parameter (as in Sec. 2.3);
5. Compute the ACF profile for each shot in a cluster and take the average;
6. Plot the ACF averages for each cluster and fit them;
7. Plot the fit results vs the time or size averages in each cluster.

The number of analyzed inside and outside shots is shown in Tab. 2.1. Let us now discuss the

$\Omega_R/2\pi$ [Hz]	# all shots	# inside shots	# outside shots
300	1491	1435	938
400	660	604	489
600	718	561	717
800	159	117	159

Table 2.1: Number of shots selected for the ACF computation. The inside shots must have  $x_2 - x_1 > 4W$ , while the outside ones must have both  $x_1 > 4W$  and  $400 \mu\text{m} - x_2 > 4W$ . It is noticeable that the inside data for 300 Hz is way bigger than the rest.

results by starting from the inside analysis and then proceeding with the outside one.

**Inside** The ACF outside profiles can be fitted with a damped cosine of the form

$$\mathcal{A}_{\text{fit}}(x) = (1 - \Delta) \cos\left(\frac{\pi x}{\ell_2}\right) \exp\left[-\frac{1}{2}\left(\frac{x}{\ell_1}\right)^\alpha\right] + \Delta, \quad (2.5)$$

with the fit parameters being  $\ell_1$ ,  $\ell_2$  and  $\Delta$ . The  $\ell_1$  parameter provides information on the length scale of the damping due to noise or, in other words, it gives a characteristic length at which the signal loses its information on being periodic.  $\ell_2$  indicates instead the length scale of the spatial patterns in the signal, as shown in App. A. The offset  $\Delta$  is a measure of how much the signal is uniformed, in fact in the limit case of a constant signal,  $\Delta = 1$  and  $\mathcal{A}(x) = 1 \forall x$ . Lastly, the exponent  $\alpha = 1.7$  was fine-tuned in order to capture the profile in the best way possible.<sup>3</sup> One could theoretically set  $\alpha$  as a fit parameter, but this would result in a worse estimation of the length  $\ell_1$ , with the fit that adapts to the data by changing only  $\alpha$ .

An example of fit on the ACF average profiles of the inside shots is presented in Fig. 2.9, where the shots are clustered by size. Due to the noise of profiles with a little number of shots, except from  $\Omega_R/2\pi = 300$  Hz the fits are performed until  $\Delta x = 11 \mu\text{m}$ . Sometimes the estimation of  $\ell_2$  fails, it is then set to  $\ell_2 = 12 \mu\text{m}$  and the fit is repeated for the other parameters.

The parameters retrieved from the fits are in Fig. 2.10, along with the ones from the fits on time-clustered data in 2.11. The size dependence seems to be the most noticeable. The offset  $\Delta$  is clearly increasing (note the clean data of 300 Hz, where the number of shots is bigger) and approaching the value of 1. As mentioned before, this means that when the bubble grows in size its magnetization becomes more uniformed, the system progressively loses local information and its periodic structures disappear. The length  $\ell_1$  is constant and bigger than the spin healing length  $\xi_s \approx 0.8 \mu\text{m}$  of Eq. (1.8). The length  $\ell_2$  does not show a clear trend.

Eventually, a global fit on all shots with the same radiation coupling is made and shown in Fig. 2.12. The  $\ell_2$  plot is not shown because its estimation succeeds only for  $\Omega_R/2\pi = 300$  Hz. Here it is interesting to notice the behavior of  $\Delta$  as a function of  $\Omega_R$ , because it reminds of the average domain wall width  $\langle w_D \rangle$  in Fig. 2.5, especially when looking at the strange 400 Hz and 600 Hz points. The length  $\ell_1$  does not show a noticeable behavior.

<sup>3</sup>Literature suggests to use  $\alpha = 2$ , a gaussian damping.

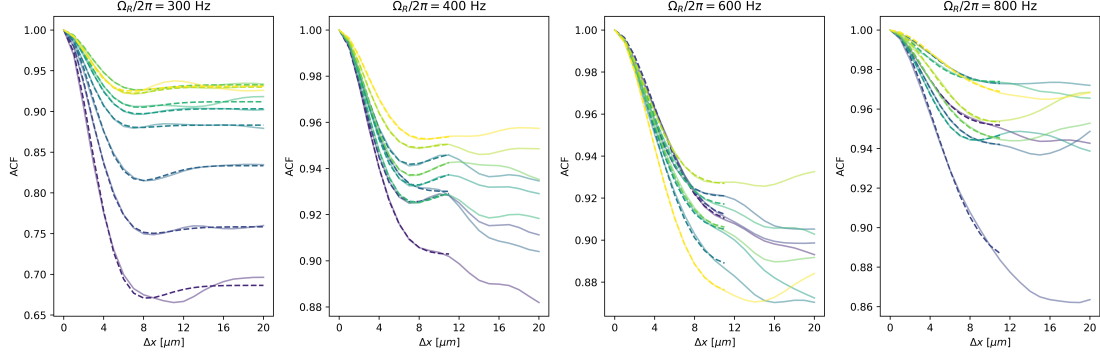


Figure 2.9: ACF average profiles of inside shots clustered by size in 9 blocks (solid lines) and fitted with the damped cosine of Eq. (2.5) (dotted lines) for each value of  $\Omega_R$ . Fits are performed until  $\Delta x = 11 \mu\text{m}$  except at 300 Hz. Size increases from darker to lighter colors.

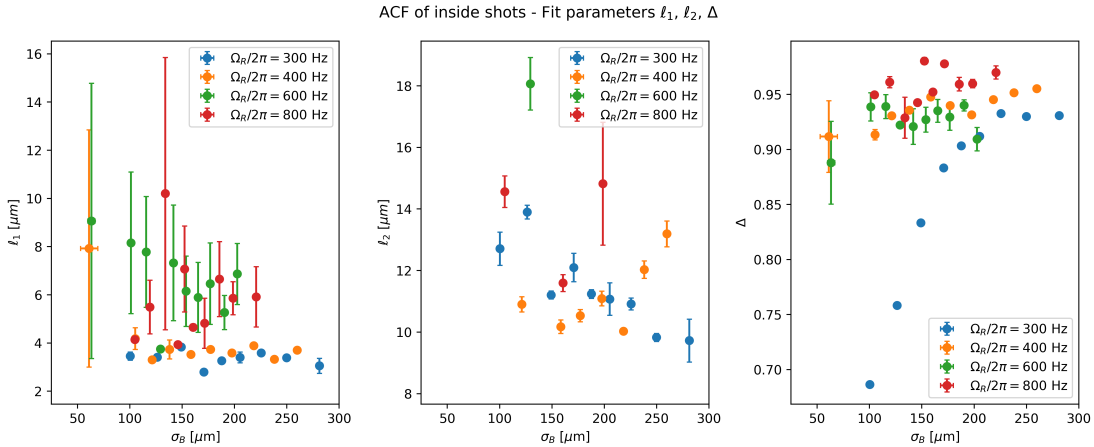


Figure 2.10: ACF fit parameters  $\ell_1$ ,  $\ell_2$  and  $\Delta$  of inside shots clustered by size. The  $\ell_2$  data when the fit fails is not shown.

**Outside** For the outside region ACF fit we prefer to use a decreasing exponential

$$\mathcal{A}_{\text{fit}}(x) = (1 - \Delta) \exp\left[-\frac{x}{2\ell_1}\right] + \Delta. \quad (2.6)$$

The reason is that the outside region does not show any particular patterns and the ACF profiles are very noisy. An example of fit (performed until  $\Delta x = 11 \mu\text{m}$ ) on the outside shots is presented in Fig. 2.13, where the shots are clustered by size as in Fig. 2.9. The parameters retrieved from the fit are in Fig. 2.14, along with those from the time-clustered data in 2.15. What emerges outside of the bubble is that the offset  $\Delta$  is decreasing with size, while  $\ell_1$  remains constant like in the inside. The decrease of  $\Delta$  is the exact opposite behavior of the inside region, where the offset increases with the bubble size. The meaning of this is that outside of the bubble structures begin to appear and it is possible that the system during the bubble expansion acquires information that was previously stored inside.

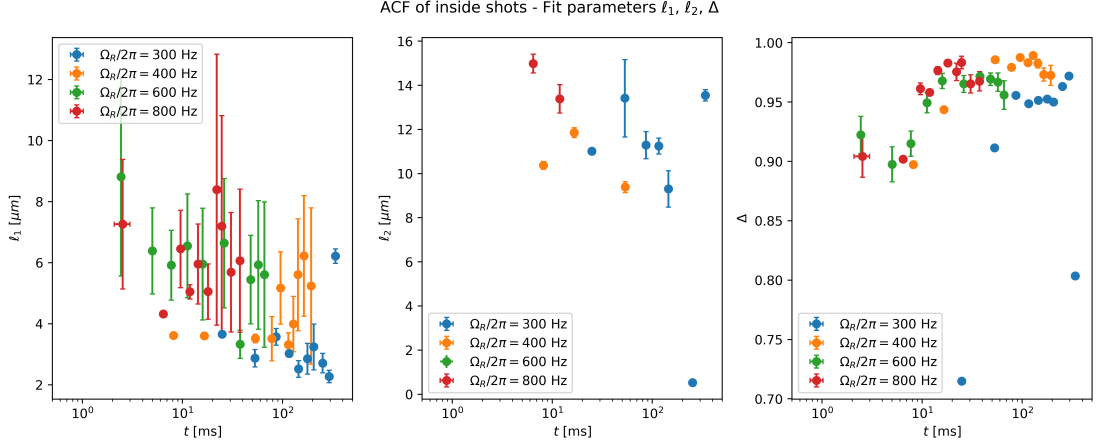


Figure 2.11: ACF fit parameters  $\ell_1$ ,  $\ell_2$  and  $\Delta$  of inside shots clustered by time (in log scale). The  $\ell_2$  data when the fit fails is not shown.

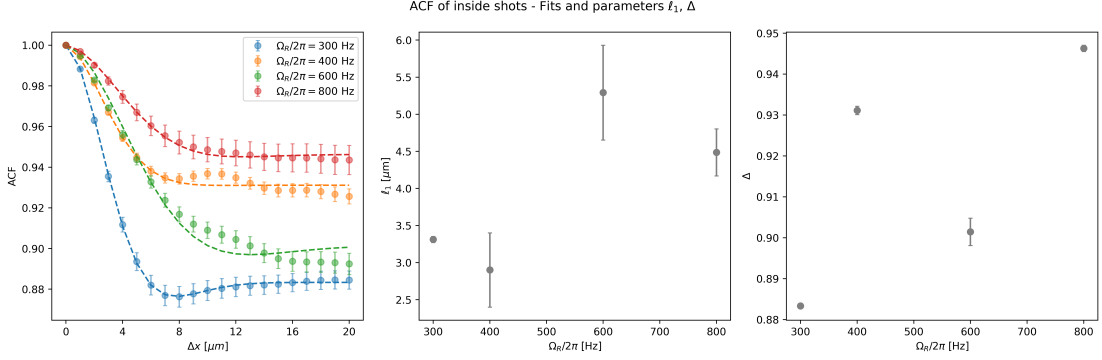


Figure 2.12: On the first plot from the left, ACF average profiles of inside shots grouped by  $\Omega_R$  (solid lines) and fitted with the damped cosine (dotted lines). Errors are estimated with the standard deviation of the ACF values. On the other plots, fit parameters  $\ell_1$ ,  $\ell_2$  and  $\Delta$  vs  $\Omega_R$ .

A global fit on all shots with the same radiation coupling is in Fig. 2.16. Here, we plot the length  $\ell_1$  against  $1/\sqrt{\Omega_R}$  and we observe that the two quantities are correlated. Furthermore, by looking at Eq. (1.8), it is the Rabi healing length  $\xi_R$  that scales in this manner, and after plotting it we see a clear correspondence between  $\xi_R$  and  $\ell_1$ , hence we can suggest that the system, outside of the bubble, has a typical length of information equal to its Rabi healing length.

## 2.4. SPECTRAL ANALYSIS

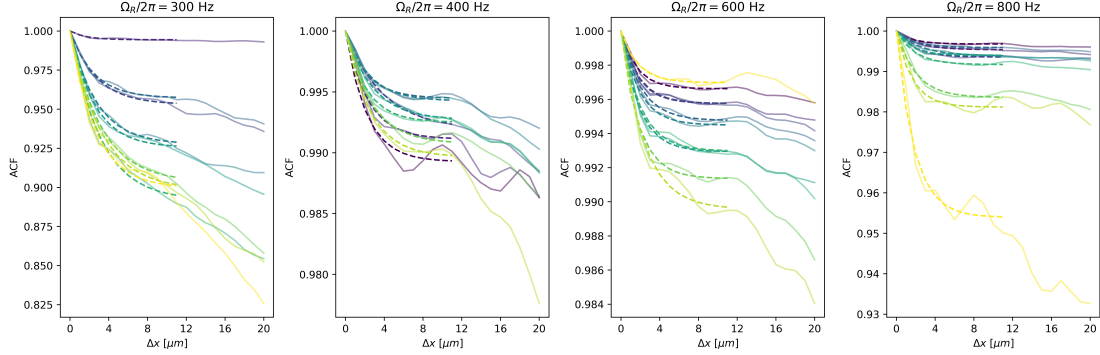


Figure 2.13: ACF average profiles of outside shots clustered by size in 9 blocks (solid lines) and fitted with the exponential of Eq. (2.6) (dotted lines) for each value of  $\Omega_R$ . Fits are performed until  $\Delta x = 11 \mu\text{m}$ . Size increases from darker to lighter colors.

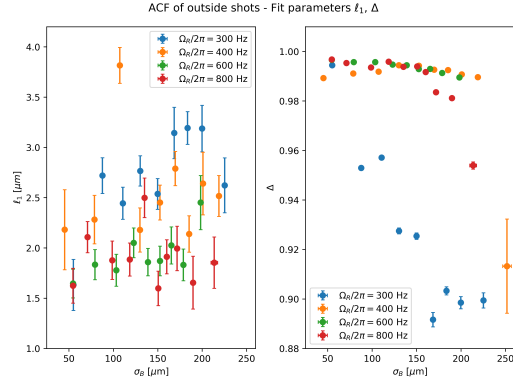


Figure 2.14: ACF fit parameters  $\ell_1$  and  $\Delta$  of outside shots clustered by size.

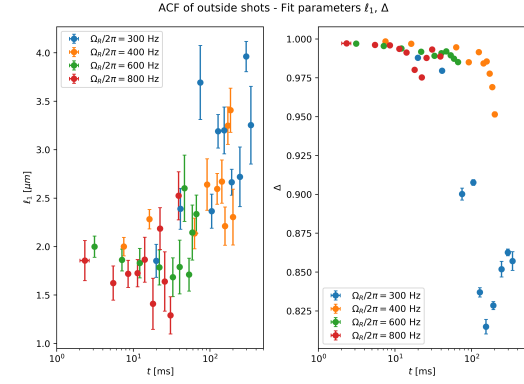


Figure 2.15: ACF fit parameters  $\ell_1$  and  $\Delta$  of outside shots clustered by time (in log scale).

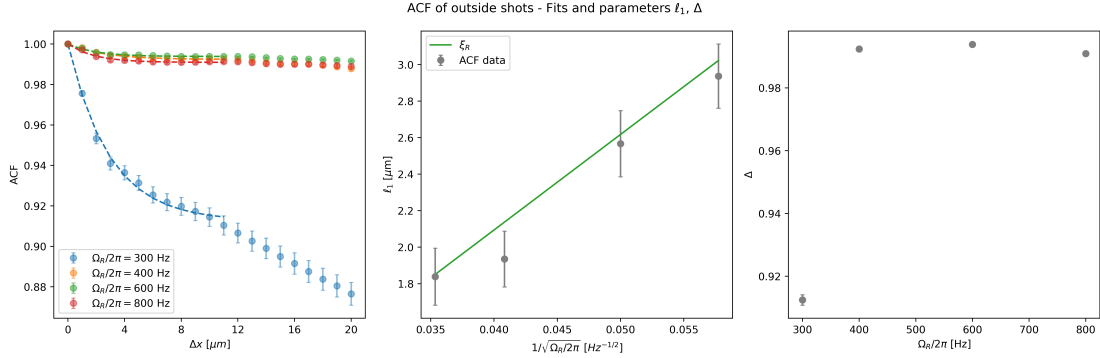


Figure 2.16: On the first plot from the left, ACF average profiles of outside shots grouped by  $\Omega_R$  (solid lines) and fitted with the damped cosine (dotted lines) until  $\Delta x = 11 \mu\text{m}$ . On the other plots, fit parameters  $\ell_1$  vs  $1/\sqrt{\Omega_R}$  and  $\Delta$  vs  $\Omega_R$ . In the central plot, the Rabi healing length  $\xi_R$  is shown as a function of the coupling.

## CHAPTER 2. DATA ANALYSIS

# Conclusions

In this thesis we characterized bubbles in a ferromagnetic superfluid by analyzing experimental measurements conducted during the first observation of false vacuum decay performed by the Pitaevskii BEC Center laboratories of the University of Trento.

First, we separated the bubbles into three distinct regions: inside, outside and border. This allowed us to study separately the regions during the bubble evolution. From the raw data we extracted the bubble magnetization shots, obtained by a spin-selective imaging process. We performed two fit routines on the shots, that resulted in acquiring information about the bubble size  $\sigma_B$ , the length of the inside region and the characteristic width of the border  $w_B$ .

After that, we analyzed these parameters by clustering the data and looking at their relative dependence and at their behavior with the experimental waiting time. By looking at the dependence with the radiation coupling  $\Omega_R$ , we discovered a non-constant behavior of the average border width  $\langle w_B \rangle$ , meaning that the spatial extension of the border region depends on  $\Omega_R$ . We also fitted the bubble size vs time data, obtaining a growth factor value  $B$  constant with the coupling, suggesting an equal growing profile for the bubbles in time, independent of  $\Omega_R$ .

Subsequently, we performed a spectral analysis on the inside and outside regions, by utilizing FFT and ACF. We confronted the two methods and decided to rely on the ACF, since the information given by the FFT was dominated by the signal noise and difficult to analyze. The ACF analysis provided information on the system in relation to the bubble size and coupling strength. In the inside region, the bubble initially presents periodic structures, but with increasing size it loses them, eventually uniforming to a flat magnetization profile. The periodicity of the signal has a dependence also on  $\Omega_R$ , with a similar behavior of  $w_B$ . On the contrary, the outside region presents no structures at the beginning but acquires them with size increasing. By comparing the results in both regions, our physical intuition is that, along with its evolution, the system transfers the periodic information from the inside to the outside region. An interesting relation was found between the typical length scale of the outside region and the Rabi healing length of the coupled system and we found that the two quantities are compatible within fit errors.

Eventually, this thesis showed that the work done provided good physically intuitive results and let us explore new physical properties of bubbles in ferromagnetic superfluids by an experimental point of view. Further advancements in the research may try to confront the experimental data to numerical simulations and explore the behavior of the system at different temperatures, or to analyze the density data.

## CONCLUSIONS

## Appendix A

### ACF model

The autocorrelation function is a powerful tool for a spectral analysis of the data, since it can extract the main frequency of the signal. Let us compute the expected model for the ACF in a simple example case, using the function

$$\mathcal{A}(m) = \frac{1}{2} \left( \frac{\sum_n f_n f_{n+m}}{\sqrt{\sum_n f_n^2 \sum_n f_{n+m}^2}} + \frac{\sum_n f_n f_{n-m}}{\sqrt{\sum_n f_n^2 \sum_n f_{n-m}^2}} \right) \quad (\text{A.1})$$

and supposing to run the sums over  $N$  values covering many periods of the signal  $f(x)$ .

Let us take a pure sinusoidal signal

$$f(x) = A \cos(k_0 x + \phi),$$

where  $x$  can be discretized with  $x = x_0 + n\Delta x$ , yielding

$$f_n = A \cos[k_0(x_0 + n\Delta x) + \phi].$$

When considering Eq. (A.1), the left and right contributions shall be treated separately (the calculation is eventually the same). We then proceed with the calculation of  $S(m) = \sum_n f_n f_{n+m}$ :

$$S(m) = \sum_n A^2 \cos[k_0(x_0 + n\Delta x) + \phi] \cos[k_0(x_0 + (n+m)\Delta x) + \phi],$$

where we can use the trigonometric identity

$$\cos(\alpha) \cos(\beta) = \frac{1}{2} [\cos(\alpha - \beta) + \cos(\alpha + \beta)]$$

getting

$$S(m) = \frac{A^2}{2} \sum_n [\cos(k_0 m \Delta x) + \cos(k_0 (2x_0 + (2n+m)\Delta x) + 2\phi)].$$

The second term in the sum averages to zero, but the first one survives and does not depend on  $n$ , hence

$$S(m) = \frac{A^2}{2} N \cos(k_0 m \Delta x).$$

---

## APPENDIX A. ACF MODEL

What is left to compute are the normalization sums  $\sum_n f_n^2$  and  $\sum_n f_{n+m}^2$ . But since the cosine squared averages to  $\frac{1}{2}$  over one period, the result is straight-forward and both sums are equal to  $\frac{A^2}{2}N$ . Eventually, the ACF right term reads

$$\mathcal{A}(m) = \frac{\frac{A^2}{2}N \cos(k_0 m \Delta x)}{\sqrt{\frac{A^2}{2}N \frac{A^2}{2}N}} = \cos(k_0 m \Delta x),$$

and since  $\Delta x$  is fixed, the ACF lets us extrapolate the signal frequency  $k_0$ .

# Bibliography

- [1] R. Cominotti et al. "Ferromagnetism in an Extended Coherently Coupled Atomic Superfluid". In: *Phys. Rev. X* 13 (2 2023), p. 021037.
- [2] Riccardo Cominotti. "Experiments with Coherently-Coupled Bose-Einstein condensates: from magnetism to cosmology". PhD thesis. University of Trento, 2023.
- [3] Riccardo Cominotti et al. "Ultracold atomic spin mixtures in ultrastable magnetic field environments". In: *Europhysics Letters* 146.4 (2024), p. 45001.
- [4] A. Farolfi et al. "Quantum-torque-induced breaking of magnetic interfaces in ultracold gases". In: *Nature Physics* 17.12 (2021), pp. 1359–1363.
- [5] Giacomo Lamporesi. "Two-component spin mixtures". In: *arXiv preprint arXiv:2304.03711* (2023).
- [6] Lev Pitaevskii and Sandro Stringari. *Bose-Einstein condensation and superfluidity*. Vol. 164. Oxford University Press, 2016.
- [7] Alessandro Zenesini et al. "False vacuum decay via bubble formation in ferromagnetic superfluids". In: *Nature Physics* (2024), pp. 1–6.

## BIBLIOGRAPHY

---

# List of Figures

1.1	GPE simulation of a two-component balanced mixture in a harmonic potential. The shaded purple region shows the density distribution of population $a$ and the yellow one the population $b$ . Here, a small magnetic field is used to break the left-right symmetry. The total density profile is drawn in black. <i>From Ref. [5]. . . . .</i>	6
1.2	Phase diagram of the magnetic properties of the system, showing the magnetization of the ground state. The association between the diagram labels and the system quantities is $\alpha \rightarrow \delta g$ , $B_3 \rightarrow \delta_{\text{eff}}$ and $B_1 \rightarrow \Omega_R$ . When $ \delta g n < \hbar\Omega_R$ we are in the paramagnetic (PM) region. On the contrary, when $ \delta g n > \hbar\Omega_R$ the system can be either in the saturated ferromagnetic (SFM) region if $\delta_{\text{eff}}$ is large enough or in the ferromagnetic (FM) region. <i>From Ref. [1]. . . . .</i>	8
1.3	Ferromagnetic energy landscape and false vacuum decay via bubble formation. <i>From Ref. [7]. . . . .</i>	9
1.4	Preparation of the system in the metastable FV state by changing the detuning from a positive to a negative value until the energy configuration is the one of Fig. 1.3 at $t = 0$ . After a waiting time $t > 0$ , the system decays into the TV state. <i>From Ref. [7]. . . . .</i>	9
2.1	Separation of the system into inside and outside region by left and right domain walls for two example bubbles. The lower bubble is measured after a higher waiting time and it has a bigger size. . . . .	11
2.2	Example of fit results performed on a shot. First, the data is fitted with the double-arctangent function of Eq. (2.2), then each domain wall is fitted with a single-arctangent, namely the one of Eq. (2.3). This ensures a better estimation of the domain wall centers and thus of the bubble width. Eventually, a last fit is done with the piecewise function of Eq. (2.4), in order to capture the inside/outside discontinuity and the exponential tails. . . . .	13
2.3	Example of initial shot sorting based on experimental waiting time (on the left) and final sorting based on bubble width $\sigma_B$ (on the right) for all shots with $\Omega_R/2\pi = 400$ Hz and $\delta_{\text{eff}}/2\pi = -596.5$ Hz. The $\sigma_B$ parameter is estimated from the previous fitting procedure, and the no-bubble shots ( $\sigma_B = 0$ ) are removed from the right plot. The data is colored by mapping positive magnetization to blue and negative magnetization to red. . . . .	14
2.4	Data clustering with the K-Means algorithm and $n_{\text{clusters}} = 20$ based only on $t$ (first two columns from the left) or $\sigma_B$ (third column). The first column shows the $\sigma_B$ data on the y-axis, while the last two show the $w_D$ data. . . . .	15

LIST OF FIGURES

---

2.5	Bubble parameters distribution averaged on all shots of the same cluster. The upper panel shows, from left to right, $w_D$ vs $\sigma_B$ , $w_D$ vs $t$ and $\sigma_B$ vs $t$ (the last one in log-log scale). Errors are estimated with the standard deviation of the values in the cluster. The lower panel presents on the left the average domain wall width over all shots with the same coupling radiation $\Omega_R$ . A linear fit on the log-log increasing data is performed in order to estimate the rate of growth, shown on the right of the bottom panel. . . . .	16
2.6	Schematic representation of ACF. Boundary effects arise when computing the autocorrelation function on the whole signal (top). Since the signal is finite, the contributions on the borders are set to zero. When restricting to windowed auto-correlation, no boundary effects are present anymore (bottom). . . . .	17
2.7	Example of FFT and ACF calculated on the inside region of shots with $\Omega_R/2\pi = 400$ Hz and $\delta_{\text{eff}}/2\pi = -596.5$ Hz, after selecting the shots where $x_2 - x_1 > 4W = 80$ $\mu\text{m}$ . The values for each shot are shown in the left graphs with colormaps, while the averages on all shots are on the right. Note that before computing the transforms the data was set to zero-mean by subtracting its average. In the lower right graph, ACF computed on the true data (without the 0-mean) is shown for comparison to the other ACF profile. . . . .	18
2.8	FFT and ACF profiles (computed with zero-mean data) averaged over all sequences with the same radiation coupling $\Omega_R$ . On the top, the FFTs are plotted both in the $k$ -domain and $x$ -domain. On the bottom, the ACFs are also plotted in the two domains to match the upper panel and confront the results. The FFTs are peaked at $k_{\text{FFT}} \sim 0.01 \mu\text{m}^{-1}$ , while the first ACF peaks are at $\Delta x_{\text{ACF}} \sim 10 - 11 \mu\text{m}$ . . . . .	19
2.9	ACF average profiles of inside shots clustered by size in 9 blocks (solid lines) and fitted with the damped cosine of Eq. (2.5) (dotted lines) for each value of $\Omega_R$ . Fits are performed until $\Delta x = 11 \mu\text{m}$ except at 300 Hz. Size increases from darker to lighter colors. . . . .	21
2.10	ACF fit parameters $\ell_1$ , $\ell_2$ and $\Delta$ of inside shots clustered by size. The $\ell_2$ data when the fit fails is not shown. . . . .	21
2.11	ACF fit parameters $\ell_1$ , $\ell_2$ and $\Delta$ of inside shots clustered by time (in log scale). The $\ell_2$ data when the fit fails is not shown. . . . .	22
2.12	On the first plot from the left, ACF average profiles of inside shots grouped by $\Omega_R$ (solid lines) and fitted with the damped cosine (dotted lines). Errors are estimated with the standard deviation of the ACF values. On the other plots, fit parameters $\ell_1$ , $\ell_2$ and $\Delta$ vs $\Omega_R$ . . . . .	22
2.13	ACF average profiles of outside shots clustered by size in 9 blocks (solid lines) and fitted with the exponential of Eq. (2.6) (dotted lines) for each value of $\Omega_R$ . Fits are performed until $\Delta x = 11 \mu\text{m}$ . Size increases from darker to lighter colors. . . . .	23
2.14	ACF fit parameters $\ell_1$ and $\Delta$ of outside shots clustered by size. . . . .	23
2.15	ACF fit parameters $\ell_1$ and $\Delta$ of outside shots clustered by time (in log scale). . . . .	23
2.16	On the first plot from the left, ACF average profiles of outside shots grouped by $\Omega_R$ (solid lines) and fitted with the damped cosine (dotted lines) until $\Delta x = 11 \mu\text{m}$ . On the other plots, fit parameters $\ell_1$ vs $1/\sqrt{\Omega_R}$ and $\Delta$ vs $\Omega_R$ . In the central plot, the Rabi healing length $\xi_R$ is shown as a function of the coupling. . . . .	23